Earth and Planetary Science Letters 600 (2022) 117890

Contents lists available at ScienceDirect

Earth and Planetary Science Letters

www.elsevier.com/locate/epsl

Climatic and lithological controls on the structure and thickness of granitic weathering zones

Bradley W. Goodfellow [a,*], George E. Hilley [b]

[a] Geological Survey of Sweden, Killiansgatan 10, 22350 Lund, Sweden
[b] Geological and Environmental Sciences, Stanford University, USA

ARTICLE INFO

Article history:
Received 26 April 2022
Received in revised form 10 October 2022
Accepted 25 October 2022
Available online xxxx
Editor: A. Webb

Keywords:
biotite
chemical weathering
climate
Fe oxidation
granite
vadose zone

ABSTRACT

Weathering of granitic rock near Earth's surface is frequently initiated by oxidative dissolution of FeO in biotite through reaction with atmospheric gases and meteoric water. This oxidation is accompanied by a volumetric expansion that increases the elastic strain energy density in the rock, leading to matrix cracking that may increase water infiltration into the rock that further drives mineral dissolution. In this contribution, we use a coupled non-dimensional, 1-D reactive-transport and fracture-mechanics model to predict how varying biotite abundance and water velocity influence granitic weathering-zone structure and thickness. Weathering-zone thickness and the volume of rock within the weathering zone that undergoes oxidative dissolution increase with water velocity but decrease with biotite abundance. The extent of matrix cracking within the weathering zone mirrors the interplay between water velocity and biotite abundance but is also influenced by crystal size. Matrix cracking potentially extends to greater depths and further into the altered rock with increasing water velocity and, in coarse-crystal granitoids, with decreasing biotite abundance. Fine-crystal granitoids require higher initial biotite abundances to undergo matrix cracking but resulting weathering zones are predicted to be thinner and display a lower volume of matrix-cracked granite. Our model predicts that thicknesses and structures of granitic weathering zones, which are observed to vary from the local to global scale, are influenced by the interplay between biotite abundance, crystal size, and water velocity. The sensitivity of weathering to local variations in these factors implies that predicting details of critical zone structure may be limited by the availability of state information about the weathering rock mass, even if integrated weathering fluxes can be simply estimated.

1. Introduction

Weathering of rock provides mineral-derived nutrients to ecosystems (Chadwick et al., 1999), releases solutes to streams and oceans (Stallard and Edmond, 1983), exerts control on landscape evolution through creating erodible regolith (Riebe et al., 2015), and regulates the Earth's climate through its key role in the carbon cycle (Berner et al., 1983; Hilley et al., 2010). Physicochemical and biological processes crack bedrock in the Earth's near-surface and convert it to saprolite (chemically weathered rock with preserved original rock textures) and soil (weathered and mechanically mixed and disrupted material), which together comprise the near-surface weathering zone. Weathering zone characteristics, such as structure and thickness, reflect spatial variations in the intensity of physio-chemical weathering partly attributable to lithological properties including bedrock composition, mineralogy, crystal dimensions, mineral fabric, and cracks. These properties control vadose zone hydrology and atmospheric gas diffusion, the types and rates of weathering processes, erosivity of the regolith, and landscape evolution (e.g., Fletcher et al., 2006; Bazilevskaya et al., 2013, 2015; Riebe et al., 2017). Despite their importance, the processes that control weathering-zone thickness and structure have proven problematic to study *in situ* because the deep weathering zone is inherently difficult to access, these deep characteristics are not easily predictable from the overlying soils (Dixon et al., 2009), and important influences occur at the crystal-scale (Goodfellow et al., 2016; Shen et al., 2019). Yet, understanding these processes is also important because humans have sharply increased soil erosion rates (Wilkinson and McElroy, 2007), and the way in which rocks can subsequently be weathered dictates landscape and biogeochemical responses to these anthropogenic changes. This contribution focuses on understanding how lithological properties and climate (hydrology) interact to influence the structure and thickness of granitic weathering zones.

---

[*] Corresponding author.
E-mail address: bradley.goodfellow@sgu.se (B.W. Goodfellow).

https://doi.org/10.1016/j.epsl.2022.117890

In granitic lithologies, chemical weathering is initiated by oxidative dissolution of Fe-bearing minerals (Fletcher et al., 2006; Buss et al., 2008) and/or dissolution of Ca-bearing accessory minerals (White et al., 2005), which ultimately allows increased water flow and feldspar dissolution (especially plagioclase because it is more reactive in weathering environments, e.g., White et al., 2001). Oxidative dissolution of the major Fe-bearing minerals, biotite and hornblende, results in volumetric expansions that produce an elastic strain that can ultimately crack the rock (Fletcher et al., 2006; Goodfellow et al., 2016; Shen et al., 2019). This cracking occurs at the millimeter-to-centimeter scale, which increases porosity and permeability, concomitant with decreasing cohesive and tensile strength. This may produce corestone rinds and/or pervasive matrix disaggregation to grus comprised of quartz and residual K-feldspar (Fletcher et al., 2006; Buss et al., 2008; Goodfellow et al., 2016). The resulting increased water flow promotes further weathering of biotite to hydro-biotite and vermiculite, hornblende to smectite, and dissolution of feldspars to clay minerals ranging from smectite to kaolinite, and/or gibbsite (Dong et al., 1998; Taylor and Eggleton, 2001, p. 156). The ultimate degree to which granites weather is controlled by all these reactions, but the spatial distribution of where weathering initiates and the mechanical transformations that produce saprolite are frequently controlled by the oxidative dissolution of Fe-bearing minerals and the resulting development of cracks within the rock (Fletcher et al., 2006; Buss et al., 2008; Goodfellow et al., 2016).

Here, we explore the role of matrix cracking from oxidative dissolution of biotite in the development of granitic weathering zones. In particular, we investigate changes in the weathering zone that might be expected to result from differences in water flow rates, Fe abundances, crystal sizes, and the mechanical properties of crystal and crack-surface boundaries. To do this, we use a reactive-transport approach, coupled with a fracture mechanics model to understand the temporal development of granitic weathering zones in idealized cases that span the observed range in driving factors, such as initial Fe content (in biotite), crystal size, weathering kinetics, and climate-driven water flow. First, we develop coupled equations that link the advection and diffusion of O_2 within the water column to the *in situ* weathering of Fe within rock. We then use a simple fracture mechanics model to predict the onset of cracking at a particular scale based on the volumetric strains associated with oxidation of FeO. Next, we non-dimensionalize these equations to identify the unique variable groups that dictate system behavior and implement a MUSCL-based conservation law finite volume solution method to simulate oxidation and cracking over time. We use these model results to identify weathering-zone domains, which show varying weathering behaviors due to differences in the initial abundance of biotite-hosted Fe(II), crystal sizes in the granitic matrix, and the rates of hydration and oxygenation of the weathering zone by water transport from the surface to depth. Finally, we use these insights as an interpretive tool to qualitatively understand variations within, and between, a set of weathering zones that display varying structures and extents. The model results provide a heuristic means of resolving a wide variety of weathering behaviors observed in granitoids through consideration of crystal-scale influences of rates of Fe oxidation and rock fracturing.

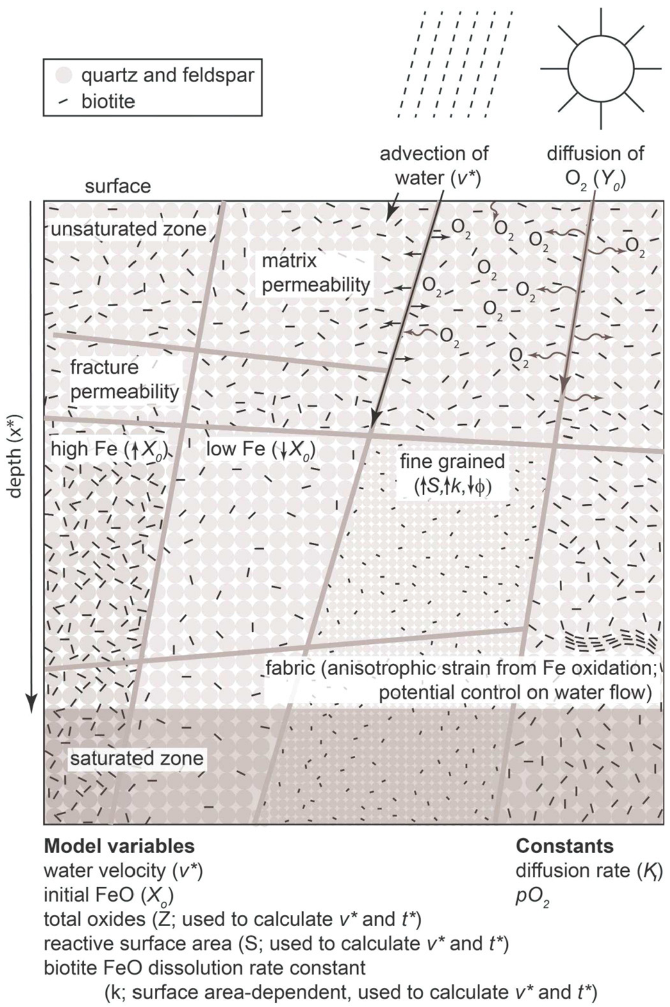

Fig. 1. Idealized weathering zone illustrating the conceptual framework for the weathering model.

2. Modeling granitic weathering zone development

We use a model-based approach to explore how granitic weathering-zone thickness and structure may vary with climatic and lithologic factors through two specific parameters: initial FeO abundance and water velocity. These parameters are proxies for initial abundance of Fe-bearing expansive minerals (Fletcher et al., 2006; Goodfellow et al., 2016) and effective precipitation, respectively. We focus on biotite because it is abundant in many granitoids. The oxidative dissolution of FeO requires the presence of O_2 and H_2O, as shown in equation (1) for the precipitation of ferrihydrite (Fletcher et al., 2006):

$$FeO + \frac{3}{2}H_2O + \frac{1}{4}O_2 \rightarrow Fe(OH)_3 \tag{1}$$

As shown in Fig. 1, water is supplied to the weathering zone by precipitation, which also contains dissolved O_2. Water flows through cracks, where it reacts with the surfaces of primary rock minerals, including biotite. The supply of O_2 to reacting mineral surfaces is supplemented by pore-water diffusion through pore spaces in the rock (Brantley et al., 2014). The O_2 in these pore spaces is replenished during periods when the weathering zone is unsaturated (Liptzin et al., 2011). Oxidative dissolution is therefore most effective in vadose zones, and the two coevolve through downwards migration of the reaction front into unweathered rock that has been advected into the weathering zone through tectonic uplift and/or stream incision (Hilley et al., 2010). Because water accesses open cracks in the granitic bedrock (Drake et al., 2009), the oxidative reaction front also moves inwards from the crack surfaces to unweathered bedrock masses bounded by the cracks (Steefel and Lichtner, 1998; Drake et al., 2009). The oxidative dissolution of FeO to $Fe(OH)_3$, shown in equation (1), is accompanied by a volumetric expansion of 4% (Fletcher et al., 2006), based on the conversion of wustite to ferrihydrite (Robie and Hemingway, 1995). Alternatively, reaction to altered biotite has been shown to be accompanied by a 5% volumetric expansion (Dong et al., 1998). These reactions increase elastic strain energy density in granitic rock, potentially generating matrix-scale cracks, which increase porosity and permeability, and thereby initiate mineral dissolution in the rock matrix.

We capture the essence of these processes using a transient one-dimensional reactive-transport model that is based on the oxidative dissolution of biotite to ferrihydrite (equation (1)) and matrix cracking through the associated increase in the elastic strain energy density. Below, we document the derivation and dimensional analysis of the model, specify the boundary conditions of the problem, and describe the method of solution of the coupled differential equations. We then link the fraction of oxidized FeO to the strain energy density changes in the modeled profile to estimate the extent to which crack surface area may be formed as the rock weathers. Finally, we use literature-reported ranges in the model parameters to develop ranges of the non-dimensional model parameters, and simulate a series of transient, one-dimensional profiles of FeO and O_2, and the extent of cracking in the weathering zone.

There are three important processes that are not treated by our current model. First, we use a simple one-dimensional approach, which does not capture the effect of lateral flow on the weathering process that may be important along slope catenas (Anderson et al., 2019). Second, we use a kinematic approach in which water velocity is prescribed and remains constant through the model run. Accordingly, we do not attempt to simulate changes in subsurface water velocities that accompany the evolution of permeability during weathering, nor do we simulate seasonal wetting and drying of the weathering zone (e.g., Navarre-Sitchler et al., 2015). Both of these factors are likely important contributors to weathering profile development but require additional parameterizations of permeability changes during weathering and a coupled saturated-unsaturated flow model approach. Finally, we do not explicitly model the weathering of non-FeO phases in the rock, which limits our approach to capturing the physio-chemical changes in the rock that occur due to volumetric expansion as FeO is oxidized.

2.1. Weathering model based on oxidation of biotite FeO

To develop our weathering model, we assign the following values:

$$X = [FeO]$$

$$Y = [O_2]$$

$$Z = [Oxide]$$

where [FeO] is the initial concentration of FeO [mol/m^3] in the granitoid, [O_2] is the initial concentration of O_2 in equilibrium with the atmosphere that is dissolved in water reacting with the granitoid [mol/m^3], and [Oxide] is the initial concentration of total oxides in the granitoid [mol/m^3]. The rate of consumption of FeO (mol/m^{3}yr) - considered stationary within the profile over time - is:

$$\frac{dX}{dt} = -\frac{k' S X^2 \phi^r Y^r}{2Zc} \tag{2}$$

where t is time (yr), k' is the biotite FeO dissolution rate constant (mol FeO/m^{2}yr), S is reactive surface area (m^2/g biotite), ϕ is porosity, r is the porosity exponent and the stoichiometric coefficient for O_2 in equation (1) (both equal 0.25: Fletcher et al., 2006), and c is the concentration of FeO per gram of biotite. The O_2 consumption rate includes terms for the downward advection of O_2 dissolved in water and diffusion of pore space O_2, and is defined as:

$$\phi \frac{dY}{dt} = -\frac{r k' S X^2 \phi^r Y^r}{2Zc} + \phi v \frac{dY}{dx} + \phi ϟ \frac{d^2 Y}{dx^2} \tag{3}$$

where v is water velocity (m/yr), x is depth (m), and $ϟ$ is the diffusion rate constant (m^2/yr).

Following Fletcher et al. (2006), we define a lumped kinetics parameter $K = k'S/c$. Substituting K into equation (2) yields the dimensional governing equations for the consumption of FeO and O_2 in our model:

$$\frac{dX}{dt} = -\frac{K X^2 \phi^r Y^r}{2Z} \tag{4}$$

$$\frac{dY}{dt} = -\frac{r K X^2 \phi^{r-1} Y^r}{2Z} + v \frac{dY}{dx} + ϟ \frac{d^2 Y}{dx^2} \tag{5}$$

We next cast equations (4) and (5) into dimensionless form. Firstly, we normalize X and Y to give non-dimensional forms of these parameters (indicated by *):

$$X^* = \frac{X}{[FeO]_0} = \frac{X}{X_0} \tag{6}$$

$$Y^* = \frac{Y}{[O_2]_0} = \frac{Y}{Y_0} \tag{7}$$

$$Y_0^* = \frac{Y_0}{X_0} \tag{8}$$

where the $_0$ subscript indicates the concentration of FeO in unweathered rock ([FeO]$_0$) and O_2 at the surface ([O_2]$_0$).

We rearrange equations (6) and (7) to define for X and Y, respectively, and then substitute for X and Y in equation (4) to yield equation (9):

$$X_0 \frac{dX^*}{dt} = -\frac{K X_0^2 X^{*2} Y_0^r \phi^r Y^{*r}}{2Z} \tag{9}$$

Dividing equation (9) by X_o yields equation (10) for the rate of consumption of X^*:

$$\frac{dX^*}{dt} = -\frac{K X_0 X^{*2} Y_0^r \phi^r Y^{*r}}{2Z} \tag{10}$$

This implies that the characteristic time (t^*) and the non-dimensional consumption rate of X^* are defined as equations (11) and (12), respectively:

$$t^* = \frac{t K X_0 Y_0^r \phi^r}{2Z} \tag{11}$$

$$\frac{dX^*}{dt^*} = -Y^{*r} X^{*2} \tag{12}$$

To define the non-dimensional consumption rate of Y^*, we return to equation (5), and substitute the definition for Y from equation (7):

$$Y_0 \frac{dY^*}{dt} = -\frac{r K X_0^2 Y_0^r \phi^{r-1}}{2Z} X^{*2} Y^{*r} + Y_0 v \frac{dY^*}{dx} + Y_0 ϟ \frac{d^2 Y^*}{dx^2} \tag{13}$$

We then cast Equation (8) in terms of X_o and substitute this into equation (13) to yield the consumption rate for Y^* shown in equation (14):

$$\frac{dY^*}{dt} = -\frac{r K X_0 Y_0^r \phi^{r-1}}{2Z} \frac{X^{*2} Y^{*r}}{Y_0^*} + v \frac{dY^*}{dx} + ϟ \frac{d^2 Y^*}{dx^2} \tag{14}$$

The characteristic length is

$$x^* = \frac{xv}{ϟ} \tag{15}$$

Substituting the definition of x in equation (15) into equation (14) yields:

$$\frac{dY^*}{dt} = -\frac{rKX_0Y_0^r\phi^{r-1}}{2Z}\frac{X^{*2}Y^{*r}}{Y_0^*} + \frac{v^2}{\varkappa}\frac{dY^*}{dx^*} + \frac{\varkappa v^2}{\varkappa^2}\frac{d^2Y^*}{dx^{*2}} \tag{16}$$

Equation (16) can be simplified to yield equation (17) for the consumption rate for Y^*:

$$\frac{dY^*}{dt} = -\frac{rKX_0Y_0^r}{2Z}\frac{X^{*2}Y^{*r}\phi^{r-1}}{Y_0^*} + \frac{v^2}{\varkappa}\left[\frac{dY^*}{dx^*} + \frac{d^2Y^*}{dx^{*2}}\right] \tag{17}$$

From equation (17), we define a non-dimensional water velocity (v^*) and the non-dimensional consumption rate of Y^* according to equations (18) and (19), respectively:

$$v^* = \frac{2v^2Z}{\varkappa KX_0Y_0^r\phi^{r-1}} \tag{18}$$

$$\frac{dY^*}{dt^*} = -r\frac{X^{*2}Y^{*r}}{Y_0^*} + v^*\left[\frac{dY^*}{dx^*} + \frac{d^2Y^*}{dx^{*2}}\right] \tag{19}$$

Our FeO oxidation model is governed by the rates of consumption of X^* and Y^*, which are defined by equations (12) and (19). In these governing equations, γ is fixed, whereas Y_0^* and v^* can vary. We define the following initial and boundary conditions for our model domain as: 1) $X(x, t=0) = X_0(x) = X_0$, such that $X^*(x^*, t^*=0) = 1$; 2) $Y^*(x^*, t^*=0) = 1$; 3) $Y^*(x^*=0, t^*) = 1$; and 4) $\frac{vY_0}{\varkappa}\frac{dY^*}{dx^*}(x^*=\infty, t^*) = 0$, such that $\frac{dY^*}{dx^*}(x^*=\infty, t^*) = 0$.

These boundary conditions require that the initial composition of rock is everywhere the same, the initial composition of oxygen in the weathering profile is everywhere equal to the prescribed concentration at the top of the profile during the model run, the concentration of oxygen at the modeled surface is held fixed at a prescribed value of $Y^* = 1$, and the rate of change of the concentration of oxygen at great depth in the weathering profile is zero. These conditions simulate the case in which oxygen enters the surface of the model, is spent by the weathering process during its transit, and does not allow upward oxygen diffusion from depth toward the surface, which are all conditions likely present in a wide variety of weathering zones.

2.2. Model of matrix cracking through oxidation of biotite FeO

Next, we develop a model for matrix cracking generated by the oxidation of biotite FeO modeled above. We consider cracking to be dependent upon the generation of a sufficient density of elastic strain energy over a length scale equivalent to the lengths of crystals comprising the granitic matrix. From Goodfellow et al. (2016) and Fletcher et al. (2006), this length scale (L, in cm) is defined as:

$$L = \frac{108\,(1-2\nu)\,\Gamma}{\xi^2 f_0^2 E}\left[\frac{V}{\Delta V}\right]^2 \tag{20}$$

where ν is Poisson's ratio, Γ is the surface energy of fracture (ergs/cm^2), ξ is the ratio of moles of FeO that have reacted to the initial moles of FeO in the rock, E is Young's modulus (dyn/cm^2), f_0 is the initial volume fraction of reacting FeO, and V is the biotite volume (cm^3). Our derivation of L is based on a cubic volume element, with fractures occurring at three faces of the cube. The shape, direction, and orientation of the fractures are therefore prescribed. Our derivation of L also does not consider plasticity. Parameter values and sources are given in Table 2. We define ξ as:

$$\xi = 1 - X^* \tag{21}$$

Equation (8) defines $Y_0^* = Y_0 / X_0$. Because Y_o is constant ($Y_o =$ 0.26 mol/m^3; Table 2), variations in Y_o^* reflect only variations in X_o We define M as the molecular weight of FeO, which is 71.85 g/mol, and rock density (ρ_{rock}) is 2.7×10^6 g/m^3. The wt% of FeO is then:

$$wt\%FeO = \frac{X_0M}{\rho_{rock}} \tag{22}$$

The initial volume fraction of reacting FeO, f_0, is defined as:

$$f_0 = [wt\%FeO]\left[\frac{\rho_{rock}}{\rho_{FeO}}\right] \tag{23}$$

where $\rho_{FeO} = 5 \times 10^6$ g/m^3. Thus,

$$f_0 = \frac{X_0M}{\rho_{FeO}} = \left[\frac{Y_0M}{\rho_{FeO}}\right]Y_0^{*-1} \tag{24}$$

$$\text{where } \frac{Y_0M}{\rho_{FeO}} = 3.172 \times 10^{-6} = k_1 \tag{25}$$

Substituting the dimensional constant k_1 into equation (24) yields:

$$f_0 = k_1Y_0^{*-1} \tag{26}$$

Substituting equation (26) into equation (20) yields:

$$L = \frac{108(1-2\nu)\Gamma}{(1-X^*)^2(k_1Y_0^{*-1})^2E}\left[\frac{V}{\Delta V}\right]^2 \tag{27}$$

From equation (27), we define the dimensional constant, k_2:

$$k_2 = \frac{108(1-2\nu)\Gamma}{k_1^2E}\left[\frac{V}{\Delta V}\right]^2 \tag{28}$$

Substituting k_2 into equation (27) permits L to be defined as:

$$L = \frac{k_2Y_0^{*2}}{(1-X^*)^2} \tag{29}$$

This implies a normalized length, L^*:

$$L^* = \frac{L}{k_2} \tag{30}$$

Substituting equation (29) into equation (30) provides the following definition for L^*:

$$L^* = \frac{Y_0^{*2}}{(1-X^*)^2} \tag{31}$$

The normalizing length-scale k_2 is bounded to a range of 4.29×10^3–6.71×10^4 m using parameter values from Table 2.

2.3. Method of solution

Equations (12) and (19) are solved with the initial and boundary conditions using a finite-volume approach, in which average quantities are simulated within volumetric elements of the simulated profile. We use a Monotonic Upstream-centered Scheme for Conservation Laws (MUSCL; van Leer, 1979) to calculate the time-derivatives of each of the quantities during each time step, which provides second-order accuracy (in space). We use a van Albada symmetric flux limiter (van Albada et al., 1982) with the MUSCL scheme. To integrate the solution forward in time, we use the LSODA ODE integration method (Petzold, 1983; Hindmarsh, 1983), which automatically selects and switches integration modes between those optimized for stiff and non-stiff problems. We use the non-dimensional water velocity with the spatial discretization length to calculate a Courant-Friedrich-Levy (CFL) limit for each simulation and restrict the integration time-step to adhere to the constraints of the CFL condition. Output from the simulations was saved at a specified time interval, where this information could

Table 1
Weathering model parameters.

Parameter	Symbol	Units	Minimum	0.5x base case	Base case	2x base case	Maximum
$FeO_{initial}$[1]	X_0	mol/m^3	185.39		729.43		1582.32
pO2[2]	Y_0	mol/m^3	0.26				0.26
Total oxides[3]	Z	mol/m^3			41271.14		
Porosity[4]	ϕ	–	0.01		0.05		0.1
Porosity exponent[2]		–	1		1		1
Diffusion coefficient[2]	D	m^2/yr	1.58		1.58		1.58
Tortuosity[2]	T	–	3		3		3
Diffusion rate[5] $\left(= D * \phi^{\frac{m-1}{T}}\right)$	Ꝁ	m^2/yr	0.53		0.53		0.53
Reactive surface area[6]	S	m^2/g biotite	0.84				4.7
Biotite FeO dissolution rate constant[6]	k	mol FeO $/m^2yr$	5.00×10^{-5}				6.29×10^{-4}
Biotite FeO dissolution rate constant	k'	mol FeO $/(m^2yr)/(mol\ O_2/m^3)^{0.25}$	7.00×10^{-5}				8.81×10^{-4}
Stoichiometric coefficient[2]	r		0.25				0.25
lumped K (K=k'S)	K	mol FeO/(g biotite yr)/$(mol\ O_2/m^3)^{0.25}$	5.88×10^{-5}				4.14×10^{-3}
c'	c'	mol biotite/g biotite	2.31×10^{-3}		2.31×10^{-3}		2.31×10^{-3}
mol FeO: mol biotite	—	–	1.5				1.5
c	c	mol FeO/g biotite	3.46×10^{-3}				3.46×10^{-3}
K/c		$1/yr/(mol\ O_2/m^3)^{0.25}$	1.70×10^{-2}		6.07×10^{-1}		1.20
Water velocity[7]		m/yr	2×10^{-2}		0.4		10
Depth	x	m	1		10		100
Time	t	yr	10^2		10^4		10^6
Initial O_2/FeO *(equation* (8))	Y_0*	Nondimensional	$\mathbf{1.64 \times 10^{-4}}$	1.78×10^{-4}	$\mathbf{3.56 \times 10^{-4}}$	7.13×10^{-4}	$\mathbf{1.40 \times 10^{-3}}$
Water velocity *(equation* (19))	$v*$	Nondimensional		$\mathbf{1.42 \times 10^{2}}$	$\mathbf{2.85 \times 10^{2}}$	$\mathbf{5.70 \times 10^{2}}$	
Depth *(equation* (15))	$x*$	Nondimensional		2.38	4.76	**9.51**	
Time *(equation* (11))	$t*$	Nondimensional		9.06	18.1	**36.2**	

Bold values are used to illustrate results in Fig. 2.

[1] Winter (2001); Migoń (2006); https://geologyscience.com/rocks/granite/.

[2] Fletcher et al. (2006) Table 1.

[3] Calculated from Winter (2001) and https://geologyscience.com/rocks/granite/.

[4] Minimum value from Fletcher et al. (2006) Table 1. The base case and maximum values are calculated from the minimum.

[5] Fletcher et al. (2006).

[6] White and Brantley (2003) Table 7; Acker and Bricker (1992); Malmström and Banwart (1997).

[7] Minimum value from Anderson et al. (2019); other values from Maher (2010).

Table 2
Cracking model parameters.

Parameter	Symbol	Units	Min	Max
Poisson's ratio[1]	ν	–	0.25	0.25
Young's modulus[2]	E	dyn/cm^2	1×10^{12}	1×10^{12}
Fracture surface energy[3]	Γ	erg/cm^2	2×10^2	2×10^3
Relative volume change[4]	$\Delta V/V$	–	0.04	0.05
Molecular weight of FeO	M	g/mol	71.85	71.85
Rock density	ρ_{rock}	g/m^3	2.7×10^6	2.7×10^6
Unit conversion constant[5]	k_1	–	3.17×10^{-6}	3.17×10^{-6}
Unit conversion constant[6]	k_2	m	4.29×10^3	6.71×10^4

[1] Fletcher et al. (2006).

[2] For granodiorite from Birch (1966).

[3] Range of values for sandstone and quartz and feldspar crystals from Brace and Walsh (1962) and Friedman et al. (1972).

[4] Fletcher et al. (2006) and Goodfellow et al. (2016).

[5] Equation (25).

[6] Equation (28).

be used for further calculating the strain energy density within the simulated profile (as described above). The code repository for the implementation of the general method and the specific models presented in this paper can be retrieved and verified from https://github.com/gehilley/NondimensionalWeathering.git.

2.4. Defining non-dimensional model parameter ranges

We use high and low end-member values from the literature for each input parameter to develop a non-dimensional base case (mean of high and low) value for initial FeO, water velocity, model domain depth, and time (Tables 1 and 2). We then double and half the base case parameters to explore the range of plausible weathering zone responses to variations in initial FeO and water velocity. Our results are cast as the extent of FeO oxidation and as matrix cracking. Whereas our model results are illustrated in one spatial dimension (top-down), this simplified representation provides some insight into the potential progression of volumetric weathering, as this weathering progresses into bedrock from crack walls that are accessible to water.

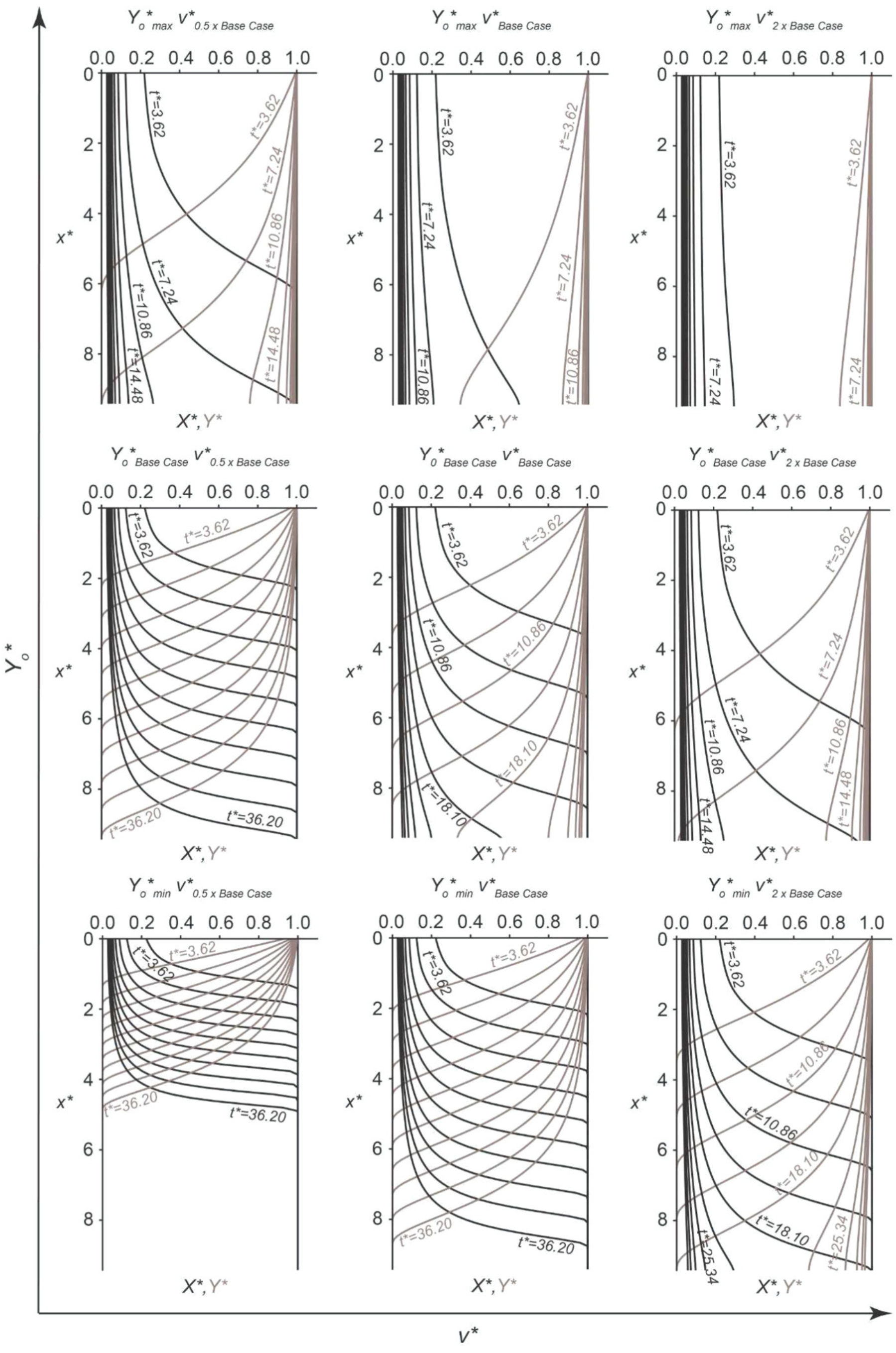

Fig. 2. Biotite weathering as a function of water velocity (v^*) and the initial ratio of O_2 (Y_0) and Fe(II) (X_0) concentrations ($Y_0^* = Y_0/X_0$). Because Y_0 is constant, Y_0^* varies as a function of X_0. Each of the nine panels shows the oxidation of Fe(II) in biotite (X^*) and accompanying O_2 depletion (Y^*) plotted against depth (x^*) at selected time slices (t^*). Water velocity (v*) is half of the base case value (Table 1) in the left-column panels and double the base case value in the right-column panels. In the top row, Y* is the maximum value (Table 1), whereas it is the minimum value (Table 1) in the bottom row. In all panels, the maximum t*, which has been divided into ten equal slices, and x* are double the base case values. Color version available as Figure S1 in the Supplement.

3. Results

3.1. Weathering model

Model results for biotite oxidation under varying water velocity and initial FeO abundance are illustrated in Fig. 2. For a given Y_0^* (which decreases as the initial abundance of FeO in the rock increases), the non-dimensional weathering depth increases for each t* value. Additionally, the length over which X* transitions from 0.0 to 1.0 increases with v* (which increases with infiltration rate). For a given v* scenario, increasing Y_0^* causes the non-dimensional weathering depth to increase at each t* value, because the O_2 consumption rate at each depth is lower than for smaller Y_0^* cases. In dimensional terms, the degree of completion of FeO oxidation at a particular depth and time increases with water velocity but decreases as the abundance of biotite increases. FeO-rich conditions produce greater pore-water O_2 consumption higher in the weathering zone at a particular time and water velocity, while depriving pore-water O_2 to the lower parts of the weathering zone. Consequently, the formation of thick zones of weathered rock is promoted by a high water velocity and a low biotite abundance, although the relatively thicker weathering zones in these cases reflect the need to access larger weathering volumes to exhaust pore-water oxygen when FeO is in short supply. Under the end-member condition of maximum water velocity and minimum biotite abundance, the Fe oxidation reaction front approaches vertical. This implies that a thick (yet sparsely weathered) zone of oxidized rock forms under this condition, in which the limited FeO reservoir is rapidly, and almost uniformly, depleted. Conversely, under the end member condition of minimum water velocity and maximum biotite abundance, the reaction front approaches horizontal as FeO oxidation rapidly consumes pore-water O_2 at higher levels in the weathering zone. This implies a much slower advance of the Fe oxidation front and a resulting thinner zone of weathered rock for a given reaction time that also displays a sharp transition to unweathered rock.

The coupled depletion of X^* and increase of Y^* is lower at a given x^* during the initial time steps of each model scenario than it is for the latter time steps (Fig. 2). Whereas the depth of X^* depletion and gradients in X^* and Y^* vary according to v^*, Y_0, and t^*, the depletion of X^* at the surface is invariant for a given time step for each model scenario. In dimensional terms, the fraction of FeO that is oxidized at the surface reflects weathering time but not the initial biotite abundance, water velocity, or the depth to which FeO oxidation extends beneath the surface.

Crystal size also controls the Fe oxidation rate. The lumped parameter, K (Table 1), displays a high value where crystal size is small because the reactive surface area displays an inverse relationship with crystal size. Because of this effect on K, a decrease in crystal size is seen from equations (10) and (17) to increase the Fe oxidation rate.

The model results shown in Fig. 2 show how weathering response varies around a base case for initial Fe abundance and water velocity derived from the literature. In contrast to the illustrated behaviors, using the low and high end-member values for the input parameters results in an all-or-nothing weathering response (Figure S2). The high end-member water velocity quickly produces a fully oxidized weathering profile, regardless of initial FeO concentration, whereas weathering is constrained to the rock surface under the low end-member water velocity, especially where the initial FeO concentration is high. Interestingly, the diversity of weathering behaviors predicted by the model is found within a more limited subset of model space, where v^* varies around its base case.

3.2. Cracking model

Cracking of the granitic matrix occurs where L^* is equal to, or less than, the dimensionless constituent crystal lengths. This occurs at different L^* values for coarse- versus fine-crystal granitoids. In particular, coarse-crystal granitoids might be expected to pervasively crack at L^* values of around 7.4×10^{-6}, while fine-crystal granitoids could undergo pervasive cracking at L^* values as low as 1.5×10^{-8} (these bounds are derived from order-of-magnitude maximum and minimum crystals lengths for granitic rocks reported in the literature; Figs. 3 and S3). The extent and depth of potential cracking of the granite matrix are controlled by matrix crystal length, water velocity, and biotite abundance, in a pattern that mirrors the extent of FeO oxidation shown in Fig. 2. A high water velocity therefore increases the rate of downwards propagation of the matrix cracking front and thereby increases the thickness of rock that may undergo matrix cracking at a given time. Increasing oxidation of FeO drives L^* towards lower values, the limit of which is determined by the initial biotite abundance. Oxidation of a high initial abundance of biotite drives L^* toward a low value, which produces a sharp vertical separation of a zone of matrix cracking near the surface from a weakly weathered zone at depth for a wide variety of granite crystal sizes. This sharp transition from cracked to intact rock slowly propagates into the largely intact rock below as the zone of O_2 consumption remains restricted to the interface between these two states. Conversely, a low initial biotite abundance limits L^* to higher values within the matrix cracking range, even when the initial reservoir of FeO has been fully depleted through oxidation. When $Y_0{}^*$ is large, the dearth of FeO in the rock prevents matrix fracturing in all but the coarsest granitoids. Even for the lowest plausible $Y_0{}^*$ case explored (Figure S3), elastic strain energy appears insufficient to crack the matrix of the finest-crystal granitoids with the highest fracture energy that we consider. Thus, the initial biotite abundance and crystal-size of the granitoid may be important determinants of whether matrix cracking is possible, even in the limiting case in which all FeO is oxidized.

The ways in which water velocity (represented by v^*), initial biotite abundance (encapsulated in $Y_0{}^*$), crystal diameter, weathering depth (represented by x^*) and time (represented by t^*) play off against one another are complex, as can be seen in Figs. 3 and S3. As an example, a coarse-crystal granitoid, with a low abundance of biotite, is predicted to undergo matrix cracking to a greater depth at a given time than a fine-crystal granitoid with a higher initial biotite abundance. These traits occur, firstly, because L^* decreases as FeO is oxidized and so first attains a length scale equivalent to larger crystals. Secondly, L^* can reach lower values in biotite-rich granitoids than are possible in biotite-poor granitoids, which increases the time required for advance of the cracking front. Thick weathering zones, comprised of grus derived from matrix cracking, can form quickly in biotite-poor coarse-crystal granitoids. However, fine-crystal granitoids require abundant biotite for sufficient strain energy to be generated to induce matrix cracking and therefore might ultimately weather more slowly, despite large reactive surface areas of small biotite and other constituent crystals, because porosity and permeability remain relatively low.

4. Discussion

Our model predicts that water velocity and mineralogy may play off against one another to cause the depth and character of granitic weathering to potentially vary over short (10^{-2} – 10^{1} m) distances. The depth of weathering generally increases with water velocity and time because both factors increase the transport of H and O ions into the subsurface that facilitates oxidation. Water velocities are controlled by climate and crack characteristics and spatial variations in these contribute to spatial variations in granitoid weathering. Spatial heterogeneity is further enhanced by matrix-scale features, including the initial abundance of FeO and crystal dimensions, which control the progression of oxidation and matrix cracking into the rock. In Fe-poor granitoids, biotite is expected to be oxidized to greater depths for a given time and water velocity, because the oxidants are more slowly exhausted than in granitoids with abundant FeO. In Fe-rich granitoids, thin zones of weathered rock displaying a high degree of disaggregation through matrix cracking may abruptly transition to unweathered rock because pore-fluid oxidants are consumed within a narrow zone. Thick weathering zones consisting of disaggregated matrix may rapidly form on coarse-crystal Fe-poor granitoid. In some contrasting cases, Fe oxidation may be insufficient to cause widespread matrix cracking. In these cases, weathering is slight and may be limited to Fe-oxide staining of otherwise hard intact rock. These interactions between water velocities, initial FeO concentrations, and crystal dimensions may help to explain why heterogeneous weathering zones in granitoids are frequently observed (e.g., Migoń and Thomas, 2002).

Our model predictions are conceptually illustrated in Fig. 4, where each panel gives an example of how biotite and water might influence granitic weathering zone development under varying spatial scales and climates. Fig. 4a shows how crystal size vari-

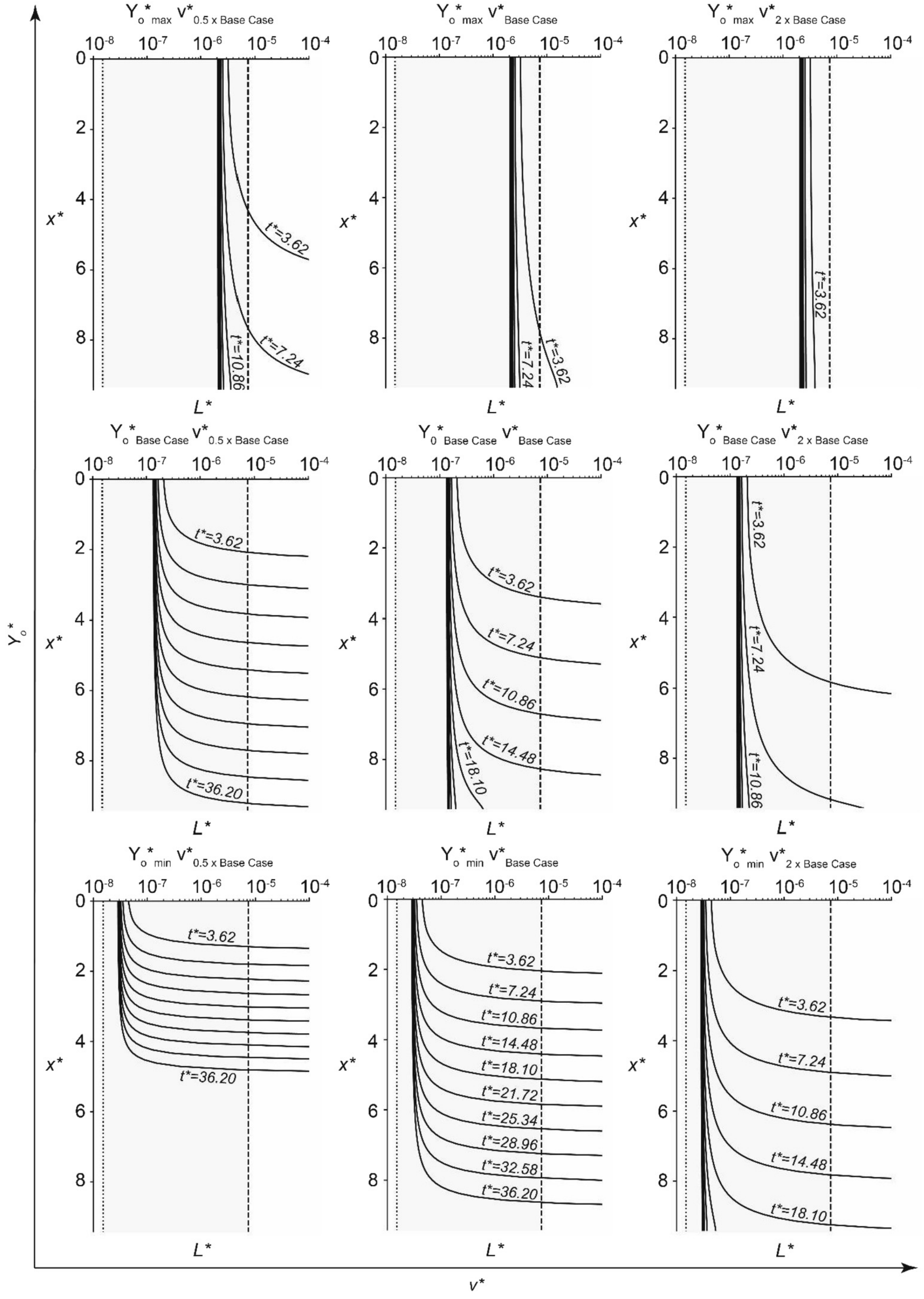

Fig. 3. Matrix cracking from biotite oxidation expressed as the length scale of cracking (L*) versus depth (x*). Water velocity (v*) is half of the base case value (Table 1) in the left-column panels and double the base case value in the right-column panels. In the top row, Y_0^* is the maximum value (Table 1), whereas it is the minimum value (Table 1) in the bottom row. In all panels, t*, which has been divided into ten equal slices, and x* are double the base case values. The grey shade indicates the range of L* where matrix cracking occurs. Its minimum and maximum bounds are indicated by the dotted and dashed lines, respectively.

ations might also influence granitic weathering zone development. Here, a vein of microgranite about 10 cm broad and comprising feldspar crystals ∼2 mm in length has been intruded into coarser-crystal Cairngorm granite (feldspar crystal lengths typically 5–10 mm), in Scotland (Goodfellow et al., 2014b). Because the microgranite is intruded after the host granite has solidified (Thomas et al., 2004), it is likely to be richer in quartz but poorer in Ca-rich plagioclase (e.g., Charoy and Noronha, 1996). It also appears to be biotite-poor. The microgranite also displays macro-crack spacing of only about 10–20 cm along the strike of the vein, which is smaller than observed in the host granite. In addition to likely compositional differences to the host granite, the smaller sizes of the constituent crystals reduce connected porosity (Goodfellow et al., 2014b), as well as demand a greater extent of Fe oxidation for matrix cracking to occur. The initial abundance of Fe(II) in the microgranite might also be insufficient for matrix cracking to develop. Because of these likely compositional variations coupled with the finer crystal size, the microgranite is more resistant to disintegration to grus through matrix cracking and mineral dissolution than the coarser-crystal host granite (Goodfellow et al., 2014b). In this case, these influences dominate despite a smaller spacing of macro-cracks in the microgranite.

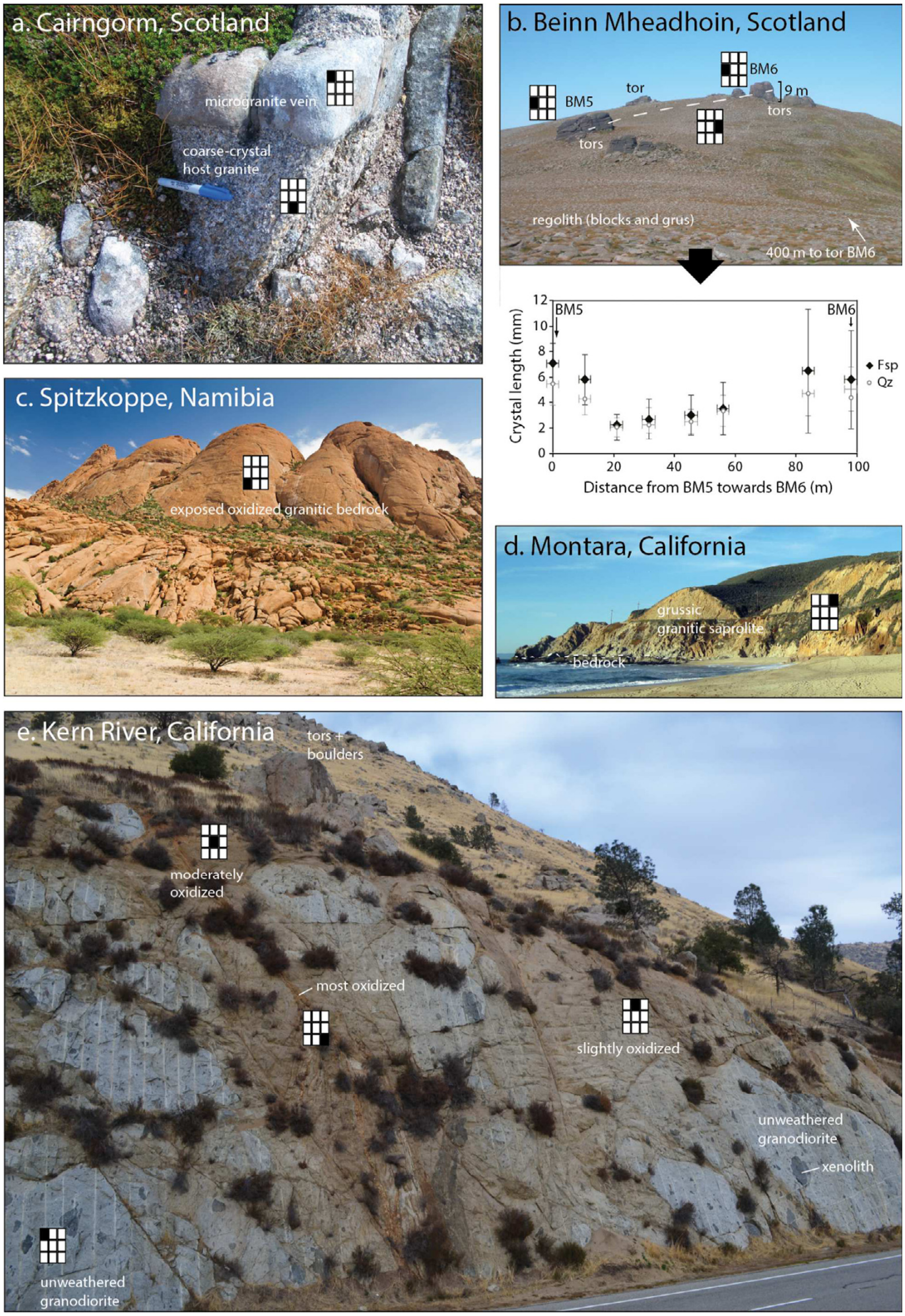

Fig. 4. Globally selected sites illustrating how the matrix cracking model may predict weathering zone thickness and three-dimensional structure. The nine panels in the matrix cracking model from Fig. 3 are represented in the photographs as a grid of nine rectangles. A particular model scenario is qualitatively represented in the photographs by a corresponding black-filled rectangle within the grid. All photographs were taken by Bradley Goodfellow, except for Spitzkoppe in Fig. 4c, which is an uncredited photograph downloaded from the web. The crystal size plot in Fig. 4b is reproduced from Figure 10b in Goodfellow et al. (2014b).

Whereas coarser crystal sizes favor matrix cracking, the influence of crystal size on granitic weathering-zone development has been shown in tor formation to be subordinate to variations in water velocity between matrix and crack permeability (Goodfellow et al., 2014b). Fig. 4b shows tors surrounded by regolith comprised of cobbles and boulders embedded in K-feldspar and quartz-rich grus on the summit of Beinn Mheadhoin, a granite massif in the Cairngorm Mountains of Scotland. Here, tors preferentially form in kernels of granite that have coarser crystals than observed in the surrounding regolith, but which also display a wider spacing of water-accessible macrocracks (Thomas et al., 2004; Goodfellow et al., 2014b). Because macrocrack permeabilities may be orders of magnitude higher than matrix permeabilities, the coarse-crystal kernels weather at slower rates than the surrounding finer crystal granite. Positive correlations between crystal size, macrocrack spacing, and tor size have been observed throughout the Cairngorm Mountains and may reflect the rate of cooling of the granites during emplacement (Goodfellow et al., 2014b). Cooling occurs heterogeneously within plutons, such that slow cooling granite kernels display both coarser crystal sizes and wider spacing of macrocracks than surrounding, more rapidly cooled, granite. These textural and deformational differences occur despite rock compositions being similar throughout the granite. Positive correlations between crystal size, macrocrack spacing, and/or tor size have been observed more generally (e.g., Ehlen, 1992; Moore, 2000, pp. 334–335), which indicates that high water velocities corresponding with high macrocrack permeability may be an important control on granitic weathering zone development and might be a dominant factor in determining weathering-zone structure for typically observed variations in crystal size.

The predicted influences of water velocity, initial Fe(II) concentration reflected in biotite abundance, and crystal size are further illustrated by comparisons of granitic weathering zone development between different regions of the globe. Figs. 4c and 4d respectively show granitic weathering under a negative annual water balance in Spitzkoppe, Namibia (mean annual precipitation (MAP)) 96 mm, mean annual temperature (MAT) 20 °C; https://www.weathertrends360.com), and a seasonally positive water balance at Montara, California (MAT 13 °C, MAP 630 mm; Climate Explorer (nemac.org)). In the image of Spitzkoppe, outcropping bedrock dominates the view, likely because the water velocity is insufficient to generate an areally-continuous regolith cover. This contrasts with weathering zone development at Montara, in which saprolite extends to tens of meters depth below interfluves to within a few meters of sea level in these coastal exposures. Corestones and surface exposures of bedrock are absent. Seasonally high water velocities may also contribute to the formation of a more homogeneous weathering zone at Montara. Whereas differences in water velocity offer the most likely explanation for the contrasting weathering zone development at Spitzkoppe and Montara, a higher abundance of biotite or a finer crystal size may also limit weathering zone thickness at Spitzkoppe.

How complex weathering zone structure may reflect spatial variations in water velocity and/or biotite characteristics is illustrated in a roadcut located in the lower Kern River canyon, California (Fig. 4e). Here annual precipitation is about 230 mm, occurring mostly in cooler months, and a distinct summer drought results in a seasonally negative water balance (Climate Explorer (nemac.org)). The weathering zone extends at least 16 m vertically but also displays a complex structure of varying weathering intensity (reflected by the intensity of Fe-oxide staining intensity and saprolite strength). In general, areas of the rock mass with high crack density appear to be most intensely weathered. In some cases, the intervening matrix is either poorly weathered or virtually unweathered, producing a series of cohesive blocks between cracks that appear to ultimately emerge on the hillslopes as boulders. These observations indicate that conditions and processes giving rise to end-member weathering conditions seen in Spitzkoppe, Namibia (Fig. 4c), and Montara, California (Fig. 4d), may vary with subtle changes in the water balance, mineralogy, and/or crystal dimensions. Thus, by using selected sites to illustrate how the model may predict weathering zone thickness and structure, Fig. 4 provides a guide as to how these predictions might be quantitatively tested. When examining both field observations and model sensitivity to water balance, biotite abundance, and crystal size, it is apparent that heterogeneous weathering of zone structures appear to be the rule, rather than the exception.

Our model illustrates the sensitivity of granitic weathering zone development to initial biotite Fe(II) concentration, crystal size, and water velocity. The predicted influence of initial biotite Fe(II) abundance is qualitatively consistent with the observation that granitic weathering zones are typically thicker than weathering zones developed on mafic rocks (Bazilevskaya et al., 2013, 2015). This difference has been attributed to variations in initial Fe(II) abundances, where lower initial abundances permit the formation of thicker weathering zones (Bazilevskaya et al., 2013, 2015), as our model also predicts for granitic weathering zones. Previous modeling studies and field observations also point to higher water velocities driving weathering zone thickening (e.g., Hilley et al., 2010; Goodfellow et al., 2011, 2014a; Anderson et al., 2019). However, global data compilations fail to indicate a clear trend of increasing granitic weathering zone thicknesses with water velocity for positive water balance locations, even when also accounting for varying initial Fe(II) abundance (Table 2.9 in Migoń, 2006; Hayes et al., 2020). This absence of a trend may reflect negative feedbacks on weathering zone thickening exerted by reducing conditions due to saturation by water and decreasing permeability due to clay precipitation. It may also reflect multiple, typically overlapping, influences on granitic weathering zone development. These influences include climate, biota, rates of uplift and erosion, topographic setting, bedrock stress conditions, and lithological properties including crack characteristics, chemical and mineralogical composition, crystal size and aspect ratio, and mineral fabric (Hilley et al., 2010; Bazilevskaya et al., 2013, 2015; Brantley et al., 2014: Shen et al., 2019; Hayes et al., 2020; Riebe et al., 2021). Finding clear evidence for the predictions of our model is impeded because the relative influences of controls on granitic weathering zone development vary spatially, but also typically over time, and some controls display threshold behavior.

There are also insufficient available field data to permit thorough testing of our model predictions. Different methods variably define weathering zone thickness (Riebe et al., 2017), which complicates inter-site comparisons, and there are essentially no data combining the relevant physical, chemical, and mineralogical characteristics in three-dimensions within granitic weathering zones. Because there are important crystal-scale controls and because controls on weathering vary over small spatial scales, it is unsurprising that in the absence of extensive documentation of these controls it is difficult to predict patterns in granitic weathering zone thickness and structure from field observations. This points to a need for controlled experiments, where weathering is documented over gradients in key factors, including relevant crystal-scale properties, in particular for biotite as highlighted by Shen et al. (2019).

Our model predictions for weathering zone development are based on variations in initial Fe(II) abundances in biotite, crystal size, and water velocity, but do not consider mineralogically controlled transience. For example, disaggregation of the matrix may create a positive feedback on feldspar and biotite dissolution rates through increasing porosity and permeability. The model also considers neither transience in strength and stiffness as the rock weathers nor transience in water velocity caused by clay mineral precipitation. Our model attributes all Fe(II) to biotite, rather than to other Fe(II)-bearing minerals that occur in granitoids, such as hornblende. The oxidative dissolution of any Fe(II)-bearing mineral should result in the same 4-5% volumetric expansion upon precipitation of Fe(III)-bearing minerals. However, because biotite is a phyllosilicate, the accumulation of elastic strain from Fe(II) oxidation will be anisotrophic, which may influence the development of the weathering zone structure through, for example, creating flow paths for water where biotite occurs as a rock fabric (Xu et al., 2022). The ratio between biotite length and thickness perpendicular to its basal cleavage also influences the rate at which rock is damaged through oxidative dissolution of biotite; the higher the biotite aspect ratio, the lower the rate of rock damage (Shen et al., 2019). Future modeling of granitic weathering zone development should target mineralogically controlled transience.

Our model highlights the key role of petrological, climatic, and macrocrack characteristics in influencing weathering zone thickness and structure. Element transfers, regardless of location in the weathering zone, are governed by the availability of weatherable minerals, atmospheric gases, and water. Therefore, in some cases, water balance may be sufficient to estimate element fluxes, integrated through the entire weathering zone (Bricker et al., 2003), to obtain solute loads (with exports from weathering zones adjusted for secondary mineral sequestration of elements). However, linking weathering processes to specific areas of the weathering zone for studies of critical zone development or formation of biologically available weathering products is dependent upon a myriad of local factors, which vary strongly in space and are difficult to predict. The implication is then that whereas calculating net element fluxes over regions may be tractable, relating those fluxes to weathering processes and locations within the weathering zone may be far more difficult because of the relevant subsurface details of the weathering zone are difficult to know without extensive three-dimensional characterization. Geostatistical characterization of these properties may be a way of estimating the heterogeneity within the weathering zone, but even so, changes in factors such as petrologic properties or crack density and orientation over short spatial scales may remain difficult to predict. Thus, while a heuristic understanding of exhumed weathering zones may be possible with the current modeling approach, predicting weathering-zone structure may be limited by the difficulty of obtaining the relative mineralogic, petrologic, and structural information about the state of the rock mass prior to weathering.

5. Conclusion

The modeling exercise explored in this work indicates that weathering zone thickness and the volume of rock within the weathering zone that undergoes oxidation increase with water velocity but decrease with biotite abundance. The extent of oxidation-induced matrix cracking within the weathering zone mirrors the interplay between water velocity and biotite abundance but is also influenced by crystal size. Matrix cracking potentially extends to greater depths and further into the weathering rock with increasing water velocity and, in coarse-crystal granitoids, with decreasing biotite abundance. Fine-crystal granitoids require higher initial biotite abundances to undergo matrix cracking but resulting weathering zones are predicted to be thinner and display a lower volume of matrix-cracked granite. Our model predicts that the thickness and structure of granitic weathering zones, which are observed to vary from the local to global scale, are influenced by the interplay between biotite abundance, structural and petrologic characteristics of the rock mass prior to weathering, and water velocity. The sensitivity of weathering to local variations in these factors implies that predicting details of critical zone structure may be limited by the availability of state information about the weathering rock mass, even if integrated weathering fluxes can be simply estimated.

CRediT authorship contribution statement

GH conceptualized the study and led model development and output. BG conducted the literature review to support model parameterization, led parameterization, wrote the manuscript and compiled the figures. BG and GH commented, edited and revised the manuscript.

Declaration of competing interest

The authors declare that they have no known competing financial interests or personal relationships that could have appeared to influence the work reported in this paper.

Data availability

Data will be made available on request.

Acknowledgements

B.G. thanks the Cox-Blaustein Fellowship for supporting costs associated with this research and the Swedish Society for Anthropology and Geography Andreéfonden for supporting costs associated with the collection and analysis of samples used in this (and earlier) research. G.H. acknowledges support provided by the Terman Fellowship. We thank Nick Hayes and an anonymous reviewer for insightful comments.

Appendix A. Supplementary material

Supplementary material related to this article can be found online at https://doi.org/10.1016/j.epsl.2022.117890.

References

Acker, J.G., Bricker, O.P., 1992. The influence of pH on biotite dissolution and alteration kinetics at low temperature. Geochim. Cosmochim. Acta 56, 3073–3092.

Anderson, R.S., Rajaram, H., Anderson, S.P., 2019. Climate driven coevolution of weathering profiles and hillslope topography generates dramatic differences in critical zone architecture. Hydrol. Process. 33, 4–19.

Bazilevskaya, E., Lebedeva, M., Pavich, M., Rother, G., Parkinson, D.Y., Cole, D., Brantley, S.L., 2013. Where fast weathering creates thin regolith and slow weathering creates thick regolith. Earth Surf. Process. Landf. 38, 847–858.

Bazilevskaya, E., Rother, G., Mildner, D.F.R., Pavich, M., Cole, D., Bhatt, M.P., Jin, L., Steefel, C.I., Brantley, S.L., 2015. How oxidation and dissolution in diabase and granite control porosity during weathering. Soil Sci. Soc. Am. J. 79, 55–73.

Berner, R.A., Lasaga, A.C., Garrels, R.M., 1983. The carbonate silicate geochemical cycle and its effect on atmospheric carbon dioxide over the past 100 million years. Am. J. Sci. 283, 641–683.

Birch, F., 1966. Rocks: elastic constants. In: Clark, S.P. (Ed.), Handbook of Physical Constants. In: Geological Society of America Memoirs, vol. 97. Geological Society of America, New York. 160 pp.

Brace, W.F., Walsh, J.B., 1962. Some direct measurements of the surface energy of quartz and orthoclase. Am. Mineral. 47, 1111–1122.

Bricker, O.P., Jones, B.F., Bowser, C.J., 2003. Mass-balance approach to interpreting weathering reactions in watershed systems. In: Drever, J.I. (Ed.), Treatise on Geochemistry, vol. 5. Elsevier, Amsterdam, The Netherlands, pp. 119–132.

Brantley, S.L., Lebedeva, M., Bazilevskaya, E., 2014. Relating weathering fronts for acid neutralization and oxidation to pCO_2 and pO_2. In: Farquhar, J., Kasting, J., Canfield, D. (Eds.), Treatise on Geochemistry. Elsevier, Amsterdam, The Netherlands, pp. 327–352.

Buss, H.L., Sak, P., Webb, R.M., Brantley, S., 2008. Weathering of the Rio Blanco quartz diorite, Luquillo Mountains, Puerto Rico: coupling oxidation, dissolution and fracturing. Geochim. Cosmochim. Acta 72, 4488–4507.

Chadwick, O.A., Vitousek, P.M., Huebert, B.J., Hedin, L.O., 1999. Changing sources of nutrients during four million years of ecosystem development. Nature 397, 491–497.

Charoy, B., Noronha, F., 1996. Multi-stage growth or rare-element, volatile-rich microgranite at Argemela (Portugal). J. Petrol. 37, 73–94.

Dixon, J.L., Heimsath, A.M., Amundson, R., 2009. The critical role of climate and saprolite weathering in landscape evolution. Earth Surf. Process. Landf. 34, 1507–1521.

Dong, H., Peacor, D.R., Murphy, S.F., 1998. TEM study of progressive alteration of igneous biotite to kaolinite throughout a weathered soil profile. Geochim. Cosmochim. Acta 62, 1881–1887.

Drake, H., Tullborg, E.L., MacKenzie, A.B., 2009. Detecting the near-surface redox front in crystalline bedrock using fracture mineral distribution, geochemistry and U-series disequilibrium. Appl. Geochem. 24, 1023–1039.

Ehlen, J., 1992. Analysis of spatial relationships among geomorphic, petrographic and structural characteristics of the Dartmoor tors. Earth Surf. Process. Landf. 17, 53–67.

Fletcher, R.C., Buss, H.L., Brantley, S.L., 2006. A spheroidal weathering model coupling porewater chemistry to soil thicknesses during steady-state denudation. Earth Planet. Sci. Lett. 244, 444–457.

Friedman, M., Handin, J., Alani, G., 1972. Fracture-surface energy of rocks. Int. J. Rock Mech. Min. Sci. 9, 757–766.

Goodfellow, B.W., Hilley, G.E., Schulz, M.S., 2011. Vadose zone controls on weathering intensity and depth: Observations from grussic saprolites. Appl. Geochem. 26, S36–S39.

Goodfellow, B.W., Chadwick, O.E., Hilley, G.E., 2014a. Depth and character of rock weathering across a basaltic–hosted climosequence on Hawaiì. Earth Surf. Process. Landf. 39, 381–398.

Goodfellow, B.W., Skelton, A., Martel, S.J., Stroeven, A.P., Jansson, K., Hättestrand, C., 2014b. Controls of tor formation, Cairngorm Mountains, Scotland. J. Geophys. Res., Earth Surf. 119, 225–246.

Goodfellow, B.W., Hilley, G.E., Webb, S., Sklar, L.S., Moon, S.G., Olsen, C.A., 2016. The chemical, mechanical, and hydrological evolution of weathering granitoid. J. Geophys. Res., Earth Surf. 121, 1410–1435. https://doi.org/10.1002/2016JF003822.

Hayes, N.R., Buss, H.L., Moore, O.W., Kram, P., Pancost, R.D., 2020. Controls on granitic weathering fronts in contrasting climates. Chem. Geol. 535, 119450.

Hilley, G.E., Chamberlain, C.P., Moon, S., Porder, S., Willett, S.D., 2010. Competition between erosion and reaction kinetics in controlling silicate-weathering rates. Earth Planet. Sci. Lett. 293, 191–199.

Hindmarsh, A.C., 1983. ODEPACK, a systematized collection of ODE solvers. In: Stepleman, R. (Ed.), Scientific Computing. In: IMACS Transactions on Scientific Computation, vol. 1. IMACS/North-Holland, Amsterdam, pp. 55–64.

Liptzin, D., Silver, W.L., Detto, M., 2011. Temporal dynamics in soil oxygen and greenhouse gases in two humid tropical forests. Ecosystems 14, 171–182.

Maher, K., 2010. The dependence of chemical weathering rates on fluid residence time. Earth Planet. Sci. Lett. 294, 101–110.

Malmström, M.B., Banwart, S., 1997. Biotite dissolution at 25 °C: the pH dependence of dissolution rate and stoichiometry. Geochim. Cosmochim. Acta 61, 2779–2799.

Migoń, P., 2006. Granite Landscapes of the World: Geomorphological Landscapes of the World, 1st edition. Oxford University Press, Oxford, UK. 416 pp.

Migoń, P., Thomas, M.F., 2002. Grus weathering mantles – problems of interpretation. Catena 49, 5–24.

Moore, J.G., 2000. Exploring the Highest Sierra. Stanford University Press, Stanford, U.S.A.

Navarre-Sitchler, A., Cole, D.R., Rother, G., 2015. How porosity increases during incipient weathering of crystalline silicate rocks. Rev. Mineral. Geochem. 80, 331–354.

Petzold, L.R., 1983. Automatic selection of methods for solving stiff and nonstiff systems of ordinary differential equations. SIAM J. Sci. Stat. Comput. 4, 136–148.

Riebe, C.S., Callahan, R.P., Granke, S.B.-M., Carr, B.J., Hayes, J.L., Schell, M.S., Sklar, L.S., 2021. Anisovolumetric weathering in granitic saprolite controlled by climate and erosion rates. Geology 49, 551–555.

Riebe, C.S., Hahm, W.J., Brantley, S.L., 2017. Controls on deep critical zone architecture: a historical review and four testable hypotheses. Earth Surf. Process. Landf. 42, 128–156.

Riebe, C.S., Sklar, L.S., Lukens, C.E., Shuster, D.L., 2015. Climate and topography control the size of sediment produced on mountain slopes. Proc. Natl. Acad. Sci. 112, 15574–15579. https://doi.org/10.1073/pnas.1503567112.

Robie, R.A., Hemingway, B.S., 1995. Thermodynamic properties of minerals and related substances at 298.15 K and 1 bar (10 (super 5) Pascals) pressure and at higher temperatures. U.S. Geological Survey Bulletin, Report, p. 461.

Shen, X., Arson, C., Ferrier, K.L., West, N., Dai, S., 2019. Mineral weathering and bedrock weakening: modeling microscale bedrock damage under biotite weathering. J. Geophys. Res., Earth Surf. 124, 2623–2646. https://doi.org/10.1029/2019JF005068.

Stallard, R.F., Edmond, J.M., 1983. Geochemistry of the Amazon: 2. The influence of geology and weathering environment on the dissolved load. J. Geophys. Res. 88, 9671–9688. https://doi.org/10.1029/JC088iC14p09671.

Steefel, C., Lichtner, P.C., 1998. Multicomponent reactive transport in discrete fractures: I. Controls on reaction front chemistry. J. Hydrol. 209, 186–199.

Taylor, G., Eggleton, R.A., 2001. Regolith Geology and Geomorphology. John Wiley and Sons, Chichester, U.K. 375 pp.

Thomas, C.W., Gillespie, M.R., Jordan, C.J., Hall, A.M., 2004. Geological structure and landscape of the Cairngorms. Scottish Natural Heritage Commissioned Report 064.

van Albada, G.D., van Leer, B., Roberts, W.W., 1982. A comparative study of computational methods in cosmic gas dynamics. Astron. Astrophys. 108, 76–84.

van Leer, B., 1979. Towards the ultimate conservative difference scheme. V. A second-order sequel to Godunov's method. J. Comput. Phys. 32, 101–136.

White, A.F., Bullen, T.D., Schulz, M.S., Blum, A.E., Huntington, T.G., Peters, N.E., 2001. Differential rates of feldspar weathering in granitic regoliths. Geochim. Cosmochim. Acta 65, 847–869.

White, A.F., Brantley, S.L., 2003. The effect of time on the weathering of silicate minerals: why do weathering rates differ in the laboratory and field? Chem. Geol. 202, 479–506.

White, A.F., Schulz, M.S., Lowenstern, J.B., Vivit, D.V., Bullen, T.D., 2005. The ubiquitous nature of accessory calcite in granitoid rocks: implications for weathering, solute evolution, and petrogenesis. Geochim. Cosmochim. Acta 69, 1455–1471.

Wilkinson, B.H., McElroy, B.J., 2007. The impact of humans on continental erosion and sedimentation. Geol. Soc. Am. Bull. 119, 140–156.

Winter, J.D., 2001. An Introduction to Igneous and Metamorphic Petrology. Prentice Hall, New Jersey, USA. 699 pp.

Xu, T., Shen, X., Reed, M., West, N., Ferrier, K.L., Arson, C., 2022. Anisotrophy amd microcrack propagation induced by weathering, regional stresses and topographic stresses. J. Geophys. Res., Solid Earth 127, e2022JB024518.